# Chapter 3

# Retrieval of Moho-reflected shear wave arrivals from ambient seismic noise

This chapter has been published as:

Zhan, Z., Ni, S., Helmberger, D. V. and Clayton, R. W. (2010), Retrieval of Moho-reflected shear wave arrivals from ambient seismic noise. Geophysical Journal International, 182: 408–420.

## 3.1 Abstract

Theoretical studies on ambient seismic noise (ASN) predict that complete Green's function between seismic stations can be retrieved from cross correlation. However, only fundamental mode surface waves emerge in most studies involving real data. Here we show that Moho-reflected body wave ($SmS$) and its multiples can be identified with ASN for station pairs near their critical distances in the short period band (1–5 s). We also show that an uneven distribution of noise sources, such as mining activity and wind-topography interaction, can cause surface wave precursors, which mask weaker body wave phases.

## 3.2 Introduction

The Green's function between two stations can be retrieved by cross-correlating extensive periods of ambient noise recordings from seismic stations (Weaver & Lobkis 2001; Snieder 2004; Wapenaar 2004). To date, geophysical studies focused on the surface wave portions of the Green's functions in the period band 5–100 s (Shapiro et al. 2005; Yao et al. 2006; Yang et al. 2007; Bensen et al. 2008; Lin et al. 2008; Zheng et al. 2008; Stehly et al. 2009). These surface waves are then used to study crustal structure (Shapiro et al. 2005; Yao et al. 2006; Yang et al. 2007; Bensen et al. 2008; Lin et al. 2008; Zheng et al. 2008; Stehly et al. 2009), site amplification factors (Ma et al. 2008; Prieto & Beroza 2008) and seismic noise source characteristics (Stehly et al. 2006; Gerstoft et al. 2008; Yang & Ritzwoller 2008). However, the body wave part of the Green's function seems to be more challenging and has rarely been reported from ASN. In the field of exploration seismology, some effort has been made to obtain reflections from ASN. Draganov et al. (2007, 2009) identified P-wave reflections from shallow reflectors (~1 km) with field data. Roux et al. (2005) reports P-wave energy in the noise cross-correlation functions (NCFs) between stations separated by 2–10 km at Parkfield, California, and Zhang et al. (2009) show that the noise is strongly correlated with ocean winds. By analysing the short period seismic noise recorded at Yellowknife array, Koper et al. (2009) show that strong energy propagates as body waves. The difficulty in retrieving body wave phases could be caused by two reasons. First, theoretical studies by Wapenaar (2004, 2006) indicate that to retrieve body wave Green's functions at the free surface requires a distribution of noise sources in depth. However, almost all the seismic noise sources are distributed on the free surface. Although the discontinuities and scatterers below the surface may help to create mirror sources or secondary sources, it is still not clear whether the body wave Green's function is retrievable under this condition. Secondly, as sta-

tions are on the free surface, we expect the Green's functions between stations to be similar to the solution to Lamb's problem, in which the surface wave is an order of magnitude stronger than body waves. This effect will be further enhanced by geometric spreading and attenuation. For example, Zhu & Helmberger (1996) show that Rayleigh waves (5–10 s) decay slower than do body waves for a large population of events recorded by a broadband regional network. However, under certain conditions such as post-critical reflections, the amplitude of body waves becomes comparable to that of surface waves at short periods (1–5 s). An example of this is the shear wave reflection from the crust-mantle transition (*SmS*) commonly observed from earthquakes. The strong amplification of this phase near the critical distance in Southern California has been suggested as the cause of particularly strong motions at large distances (Mori & Helmberger 1996).

A strong *SmS* phase requires a laterally coherent crust (Mori & Helmberger 1996) such as the Kaapvaal craton, near Kimberley, South Africa (James et al. 2003) and the Great Slave Lake region in north Canada (Viejo & Clowes 2003; Clowes et al. 2005). The presence of dense seismic arrays in these two regions makes them ideal locations to verify that we can obtain *SmS* from the NCFs. In the Great Slave Lake example, the presence of two dense arrays shows that some of the precursory arrivals are due to uneven noise source distribution, specifically noise voids caused by wind shadows.

## 3.3 Body waves from ambient seismic noise; Southern Africa

We used more than 30 broad-band stations in the Kaapvaal array and the Kimberley array (in Southern Africa Seismic Experiment) under the Kaapvaal Project (James et al. 2003) and BOSA station in global telemetered seismograph network (Figure

3.1) to look for *SmS* arrivals. The red star (Welkom) indicates the location of a mine earthquake (1999 Matjhabeng event) that was well recorded by the Kimberley Array. The broad-band array has been used to derive a detailed 1-D crustal model using the receiver function method (James et al. 2003). The model has a sharp Moho with $P$ and $S$ velocities jumping from 6.73 and 3.89 km/s to 8.20 and 4.79 km/s in less than 1 km. They used this model to compare synthetic waveforms against those produced by the earthquake with remarkable success. Not only were they able to identify *PmP* and *SmS,* but also their multiples which implies a simple Moho structure and consistent crustal thickness over long distances. A vertical velocity profile of the earthquake data is displayed in the upper half of Figure 3.2 (red). At long-periods, the Rayleigh waves are dominant, although the *Pnl* phases (in the 30–40 s window) can still be observed. These two wavetrains are commonly observed for earthquakes and modelled to determine source parameters (Zhu & Helmberger 1996). Generally, the *SmS* phase is unstable in tectonic regions, which makes the strong *SmS* arrival in craton shown in Figure 3.2 an ideal target to compare the NCFs with earthquake seismograms.

The station pairs are chosen to make SA14, SA26 and SA30 as 'pseudo-source stations' (shown as grey lines in Figure 3.1). Our procedure to compute daily NCFs is similar to that described by Bensen et al. (2007). Continuous vertical velocity records from 1999 January to 1999 June are downloaded from IRIS and cut into daily segments. After removal of mean, trend and instrumental response, the seismograms are bandpass filtered between 1 and 10 s. To remove the effect of earthquakes, we first filter the original seismograms between 15 and 50 s to emphasize the surface waves of earthquakes, and then calculate their envelope functions. The inverse of these smoothed envelope functions are used to weight the corresponding seismograms between 1 and 10 s. This procedure has been proven to be effective to suppress earthquake signals (Bensen et al. 2007). To make the cross-correlation result in 1–5 s

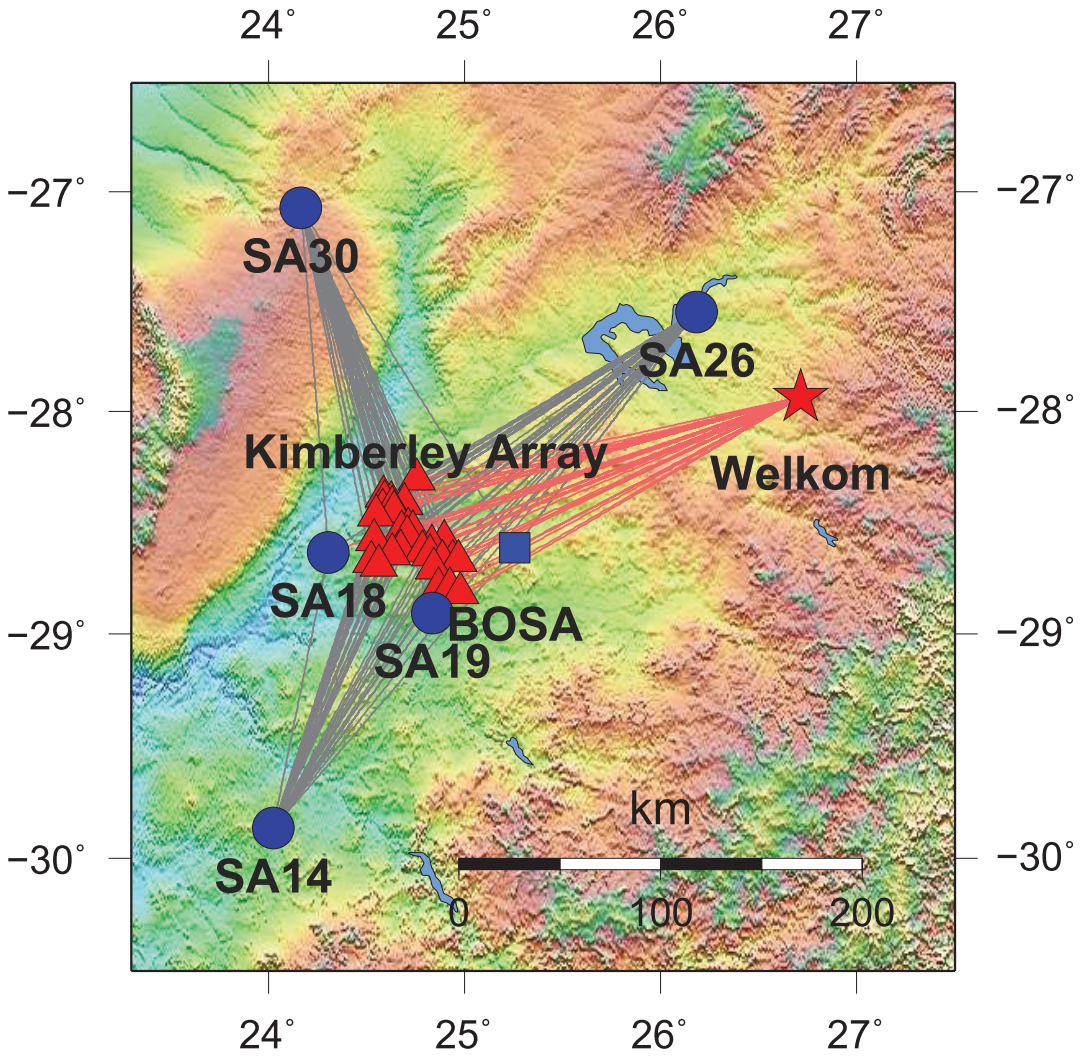


Figure 3.1: Stations used in the Kimberley region and the 1999 Matjhabeng earthquake (Welkom, red star). The red triangles indicate the Kimberley array stations. The blue dots indicate the Kaapvaal array stations and the blue square is an IRIS/GSN station. NCFs are computed along station pairs shown as grey lines, with SA14, SA26 and SA30 as 'pseudo-source stations'. The red lines indicate the paths from the earthquake to the various array stations displaying some overlap with paths from SA26.

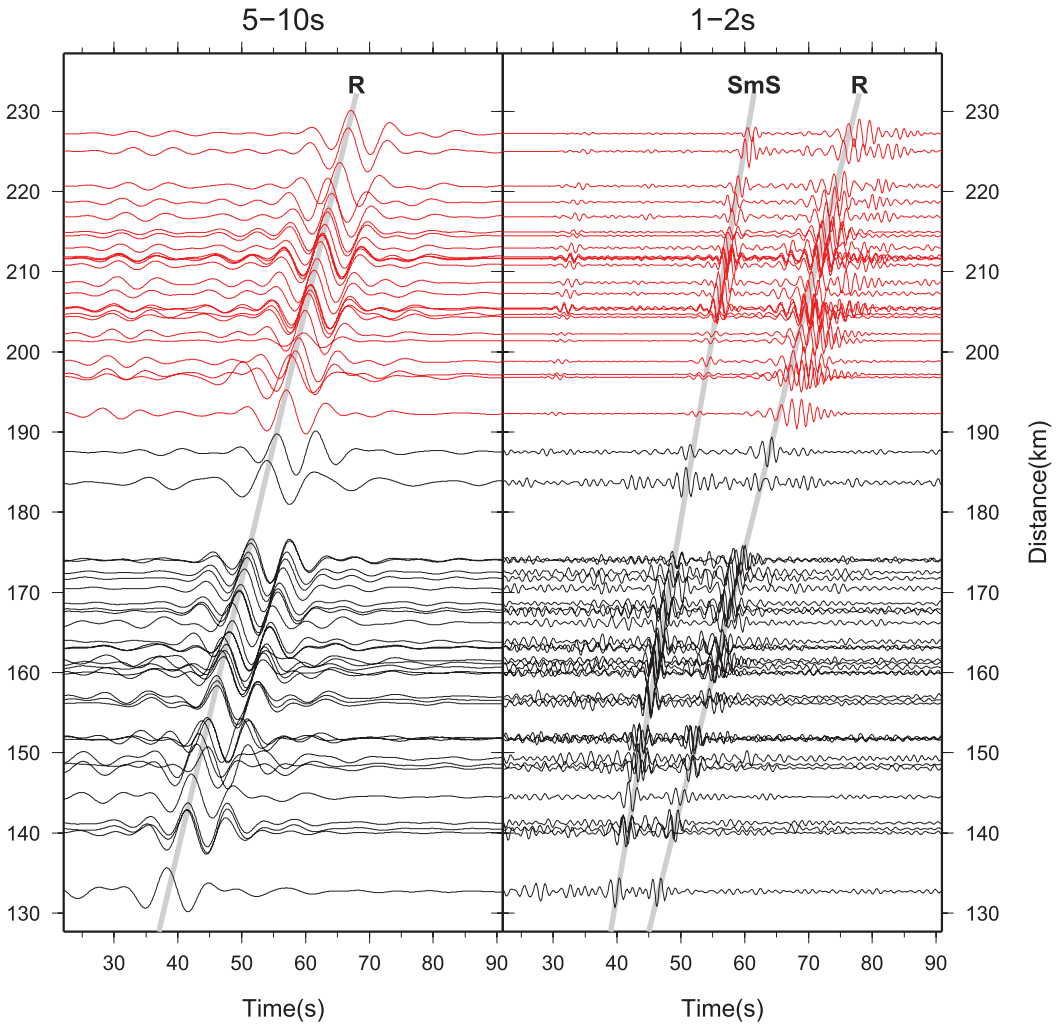


Figure 3.2: Record sections of earthquake broadband vertical velocity records (red lines) and NCFs using SA14 as the source station (black lines). The left and right panels are for 5–10 s and 1–2 s period bands, respectively. In the 5–10 s period band, Rayleigh waves for both earthquake data and NCFs are very clear. The earthquake data has been shifted 4s forward to account for the depth difference between deeper earthquake and pseudo-source station. The same time shift is then applied to the 1–2 s period band. In the 1–2 s period band, the *SmS* of NCFs are well aligned with *SmS* of the earthquake records (James et al. 2003), as well as Rayleigh waves. *SmS* is also present in NCFs with SA26 and SA30 as source stations as addressed later.

more visible, we apply a spectral whitening between 1 and 10 s because the energy in the 5–10 s period band is much stronger than in the 1–5 s band. Cross-correlation is then computed over daily intervals and stacked. All the daily NCFs are normalized to their maximum amplitude before stacking, to avoid erratic data and residual effects of earthquakes. The positive and negative sides of the stacked NCFs are folded and summed to give the final NCFs.

The lower portion of Figure 3.2 shows the NCFs with SA14 as pseudo-source station, filtered in the period bands 5–10 s and 1–2 s. As expected, in the 5–10 s period band, we can see coherent Rayleigh waves in the NCFs and the earthquake records. In the NCFs of 1–2 s, we see clear signals that are coincident with the *SmS* phase in the earthquake seismograms. This identification is confirmed by the similarity of spectrograms of the NCF and earthquake records. Figure 3.3a displays one typical NCF and its spectrogram computed with the multiple filter technique (Dziewonski et al. 1969; Levshin & Ritzwoller 2001). There are two separate wave packets in the NCF. The latter wave packet is of longer period and with an apparent dispersion typical of surface waves. The earlier wave packet in the short-period band (from about 1 to 2 s) displays no dispersion and has a group velocity of about 3.5 km/s. These features are very similar to those in the spectrogram of the seismogram recorded at one station in the Kimberley array generated by the Matjhabeng earthquake (Figure 3.3b). The *SmS* phase can also be observed at station pairs in different azimuth directions with SA14, SA26 and SA30 as source stations (Figure 3.4) and they are all travelling with approximately the same apparent velocity (3.5 km/s). As the group velocity of surface wave is about 3.0 km/s, the angle between the noise directivity and station pair needs to be very close to 31° to make a 3.5 km/s apparent velocity. For example, if the angle is 15 or 45°, the apparent velocity will be 3.11 or 4.24 km/s, which can be easily distinguished from 3.5 km/s. The azimuth range from any station of SA14, SA26 and SA30 to the Kimberley array covers more than 15°. This means

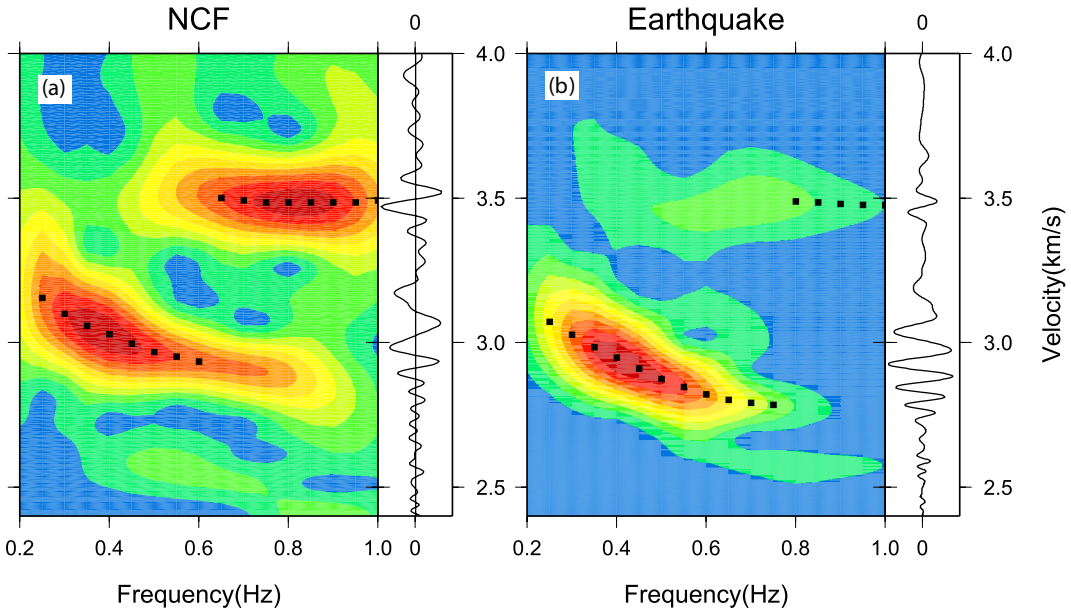


Figure 3.3: (a) One example of NCF and its spectrogram, displaying a dispersive Rayleigh wave, and a non-dispersive short period (1–2 s) signal (*SmS*) with constant group velocity (3.5 km/s). For comparison, (b) shows a seismogram due to the Matjhabeng earthquake, and its spectrogram, which has a very similar pattern of Rayleigh and body waves, thus validating the *SmS* identification.

that the *SmS* is not caused by uneven distribution of the surface wave seismic noise. The NCFs can also detect the first multiple of *SmS* ($SmS^2$) when this phase reaches the critical distance as displayed in Figure 3.5. In this case, we extended the distance to capture the strongest expected $SmS^2$, which is about two times the distance for *SmS*. Here, we see some small differences in the relative waveform packets which are to be expected at these short-periods due to the small-scale variations of Moho topography and crustal structure (Mori & Helmberger 1996).

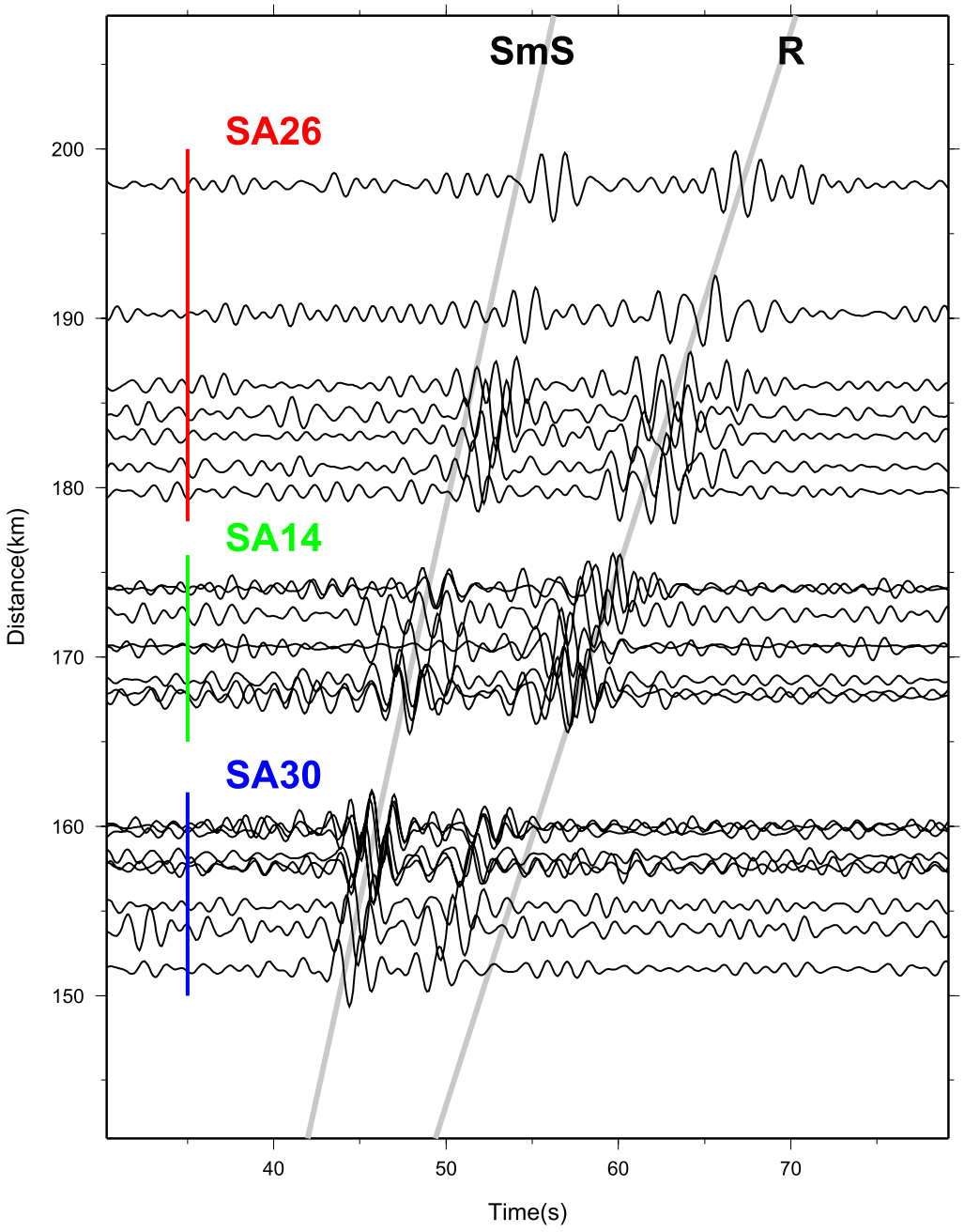


Figure 3.4: Record section generated from a composite set of paths displaying the azimuth independence of *SmS* observations. Clear *SmS* and Rayleigh waves can be seen in NCFs (bandpassed 1–2 s) with SA14, SA26 and SA30 as source stations, which sample a wide range of azimuths. It indicates that the observation of *SmS* in NCFs is independent of station pair azimuths and cannot be due to directivity of noise, which could be a problem in other regions. Not all the NCFs are shown to avoid overlapping of seismic traces.

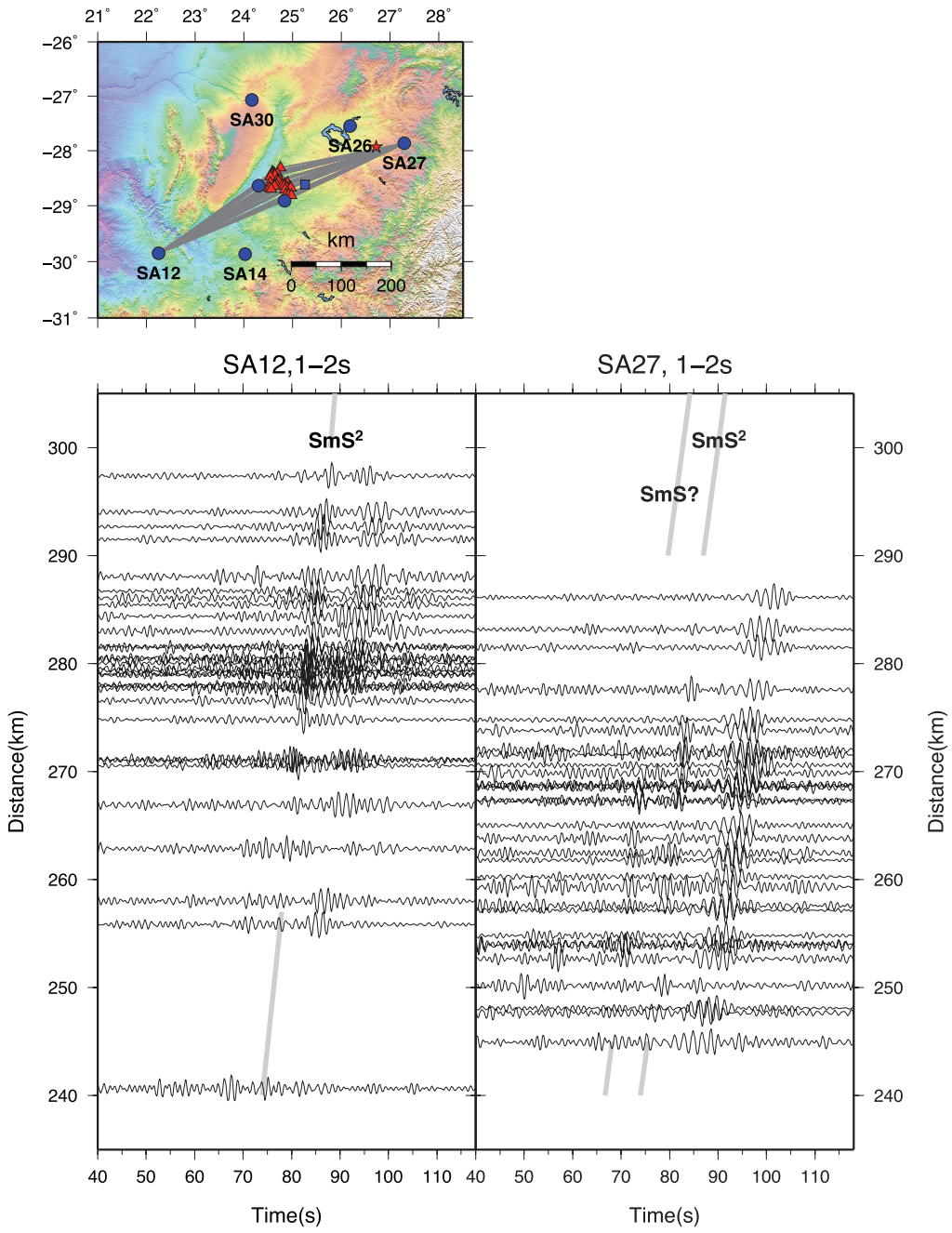


Figure 3.5: Observation of $SmS^2$ in NCFs of station pairs at larger distances with two additional pseudo source stations SA12, SA27 denoted in grey lines. The lower panel displays the NCFs at 1–2 s. At these distances, $SmS$ becomes weak and $SmS^2$ becomes the strongest body wave phase as predicted by heavy grey lines.

## 3.4 Body waves from ambient seismic noise; Northern Canada

The Great Slave Lake region of Northern Canada (Figure 3.6) is another location with simple crustal structure, that has been well determined by the LITHOPROBE seismic reflection and refraction studies (Viejo & Clowes 2003; Clowes et al. 2005). The LITHOPROBE transect covers 2000 km from the Archean Slave craton to the Pacific. A total of 37 shots were detonated and recorded by 600 instruments with average spacing of 1 km. The line starts at Yellowknife at the edge of the Great Slave Lake and crosses the CANOE array as displayed in Figure 3.6. The wide-angle reflection profile for this line shows a remarkably strong *PmP* between 100 and 200 km offset along with synthetic seismograms. As discussed in their paper, the Moho is remarkably flat with variations between 33 and 36 km, and is relatively sharp as in the above example beneath Southern Africa. The crustal model is displayed in Figure 7 where the P and S velocity jump from 6.6 and 3.8 km/s to 8.0 and 4.6 km/s at the Moho. Detailed receiver function analysis at Yellowknife array also shows a similar result (Bostock 1998). In short, this location is ideal for searching for *SmS* body waves from noise cross correlation.

Two dense arrays were deployed in the region as shown in Figure 3.6. One is the permanent Yellowknife array (YKA), and the other is the temporary CANOE array (Mercier et al. 2008). We will use these two arrays to interrogate the directional properties of the noise field and NCFs. Continuous data from May 2004 to July 2005 are downloaded from IRIS. The procedures to compute the NCFs are the same as those used in South Africa. The NCFs (bandpassed at 2–10 s) along the paths shown as grey lines in Figure 3.6 are given in Figure 3.8. Because the crustal model is known from the above study, we attempted to compare these NCFs directly with synthetic 1-D Green's functions. After some minor adjustments in the shallow velocities as

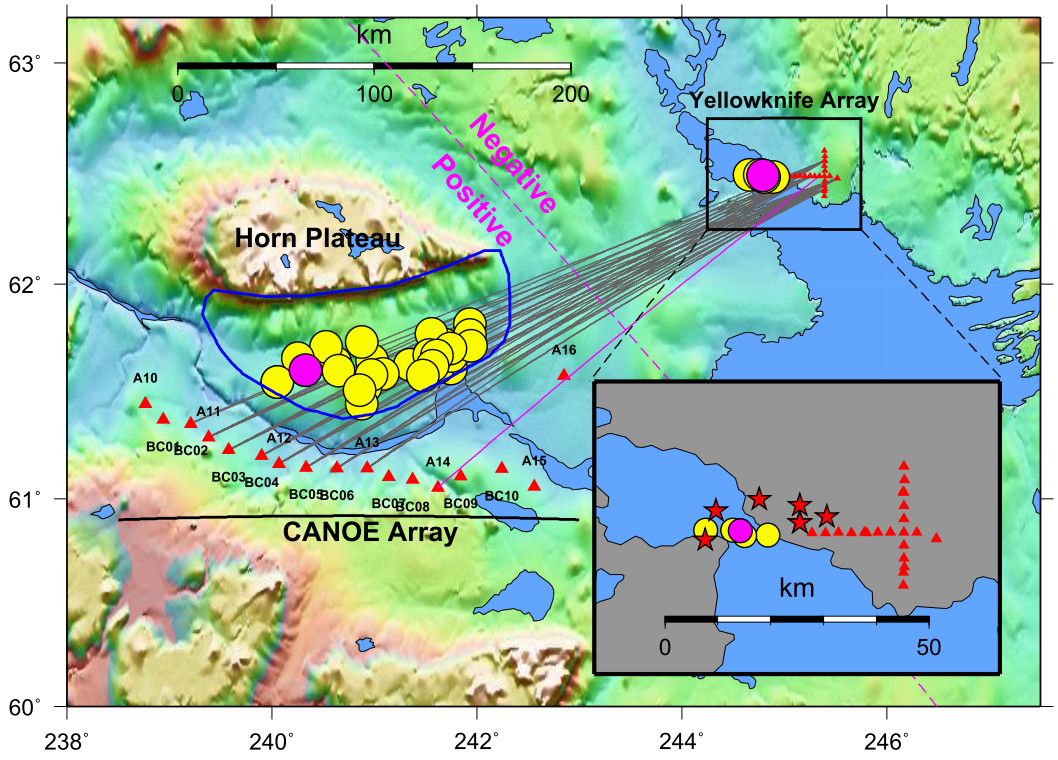


Figure 3.6: Geometry of a second ASN test involving stations (red triangles) in two arrays, a closely spaced array (Yellowknife), and a broadband array (CANOE). The grey and purple lines are the paths where NCFs have been studied. The purple dash line, which is the perpendicular bisector of the purple line (A14 to YKA), separates the noise sources contributing to the positive or the negative side of the NCF with A14 as the pseudo-source. The purple and yellow dots indicate the locations of identified noise source anomalies (NSAs). The left group of dots to the south of large topographical feature Horn Plateau lie in the approximate area with much lower annual average wind speed than surrounding area (blue curve, data from Canada Environment 2009). The right group of dots coincides with known mining blasts in 2004 and 2005 reported by Earthquakes Canada (red stars in the inset).

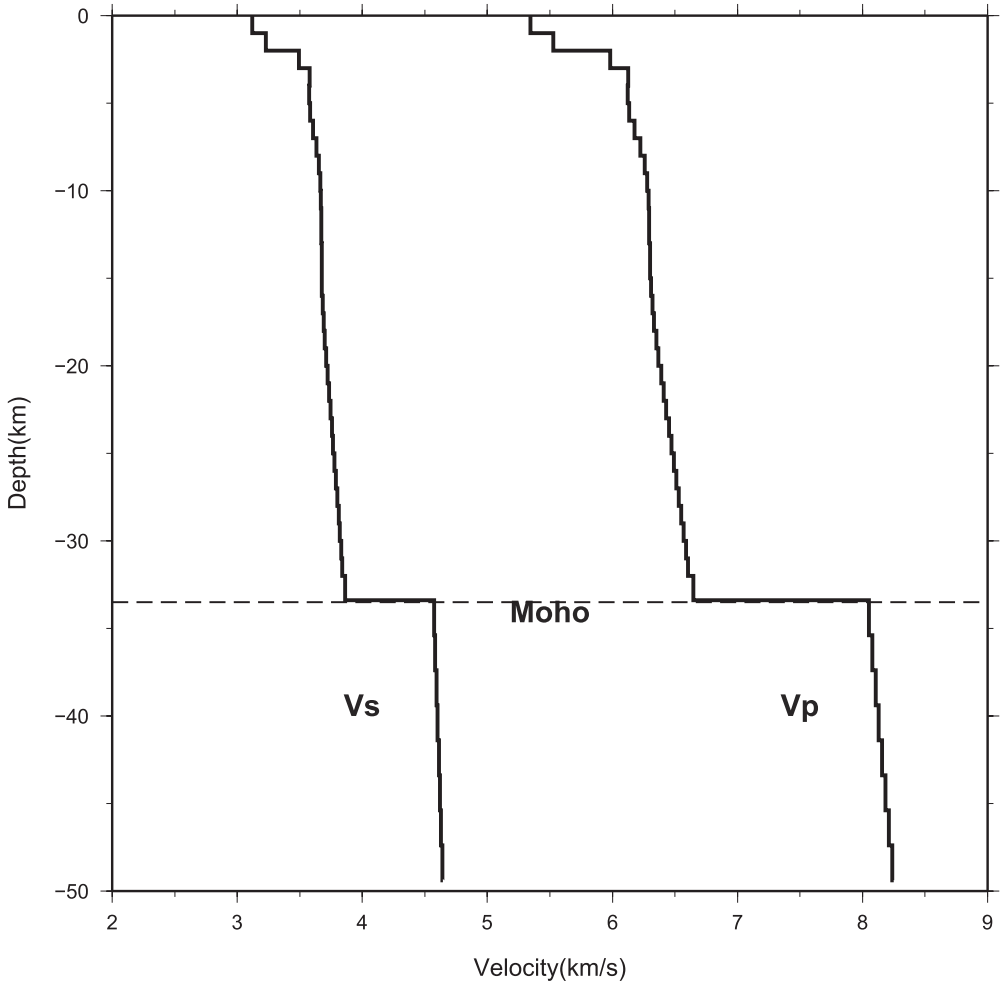


Figure 3.7: 1-D Vp and Vs model used to calculate the synthetic seismograms. This model is averaged from SNORE' 97 (Viejo & Clowes 2003; Clowes et al. 2005) and then modified for the top 5 km (where the wide-angle reflection experiment has little resolution) to fit short period surface waves.

given in Figure 3.7, we obtained the match displayed in Figure 3.8. These synthetics were generated with a frequency–wavenumber (w-k) synthetic seismogram package (Zhu & Rivera 2002) assuming the source station is replaced by a vertical point force. The distances between stations here are from 280 to 350 km, which is beyond the critical distance range of *SmS*, but falls in the critical distance range of $SmS^2$. The synthetic Green's functions match both surface waves and $SmS^2$ body waves very well. Figure 3.9 shows the comparison of NCFs and synthetic Green's functions over the paths with shorter distances (150–180 km) where SmS is in the critical reflection range. Station A16 is the only station at this distance range to YKA. The synthetics (red) are computed with the same 1-D crustal model and w-k code as in Figure 3.8. The fit to the *SmS* is again excellent confirming our identification of body waves retrieval from noise analysis. The fit to the surface waves in this case is disturbed by the slightly shorter period (2–5 s, rather than 2–10 s to avoid the interference between Rayleigh waves and *SmS*) and possible lateral heterogeneity of shallow structure. Note that the *SmS* is not sensitive to the shallow structure as the nearly vertical path through it is only a very small fraction of the entire path.

These two examples in South Africa and Northern Canada demonstrate definitive observations of *SmS* and $SmS^2$ from ASN when they have large amplitudes near their critical distances. This means that although almost all the noise sources are distributed on the free surface, there seems to be no difficulties in retrieving body waves from ASN when they are supposed to have large amplitudes in the Green's functions. In the next section, we will discuss problems in obtaining other weaker body wave phases, which may be masked by the waves in NCFs which are neither surface wave nor body wave phases.

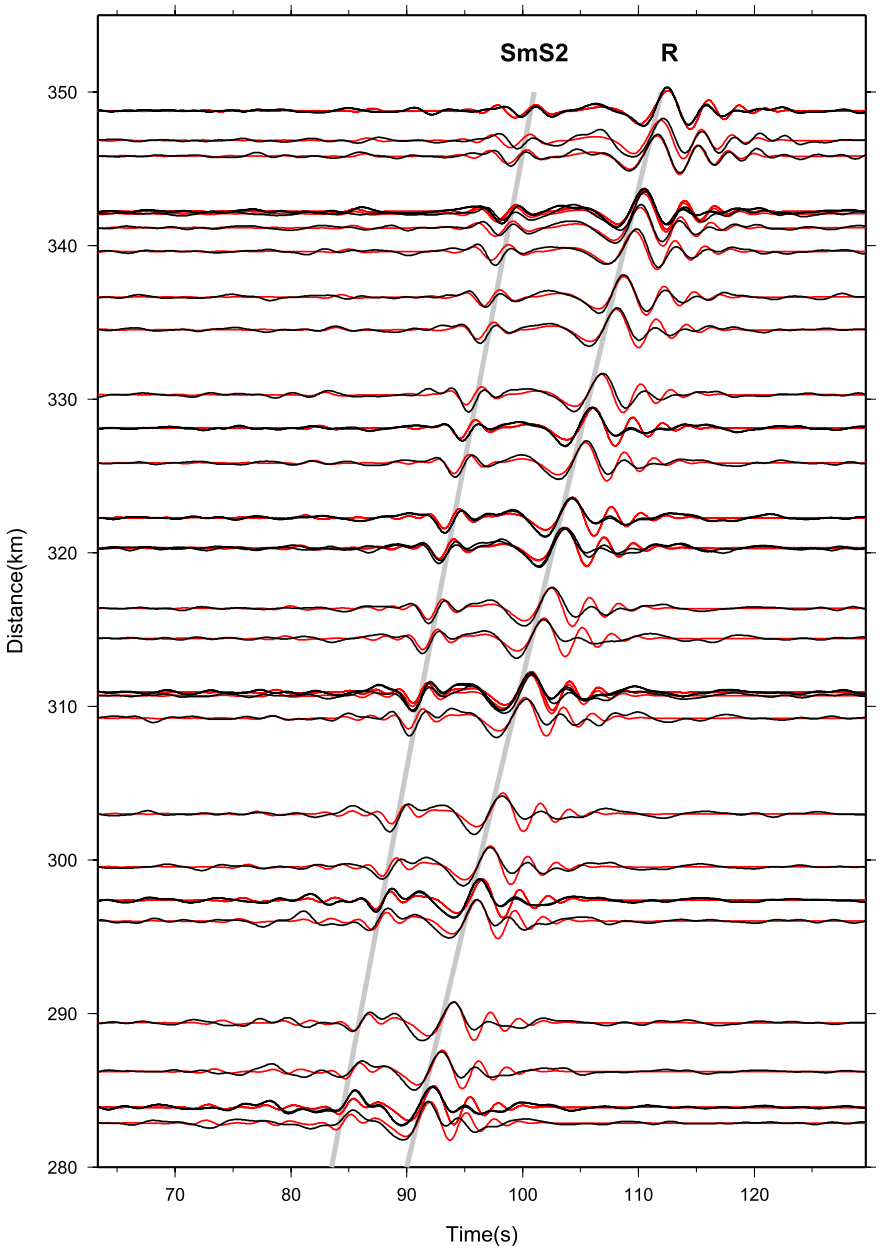


Figure 3.8: Comparison of synthetic Green's functions from a known structure with noise cross-correlation functions (NCFs) near Great Slave Lake. The black lines are NCFs of station pairs shown as gray lines in Figure 3.6 with distance range from 280 to 350 km. More complete NCFs (with NCFs between all station pairs) are addressed later. The red lines are synthetic seismograms with a single vertical force at one station, recorded at the other station. The seismic 1-D model is taken from Viejo & Clowes (2003) and Clowes et al. (2005), shown in Figure 3.7. At this distance range, the two most visible phases are $SmS^2$ and Rayleigh waves. The great agreements between NCFs and synthetics indicate definitive identification of $SmS^2$.

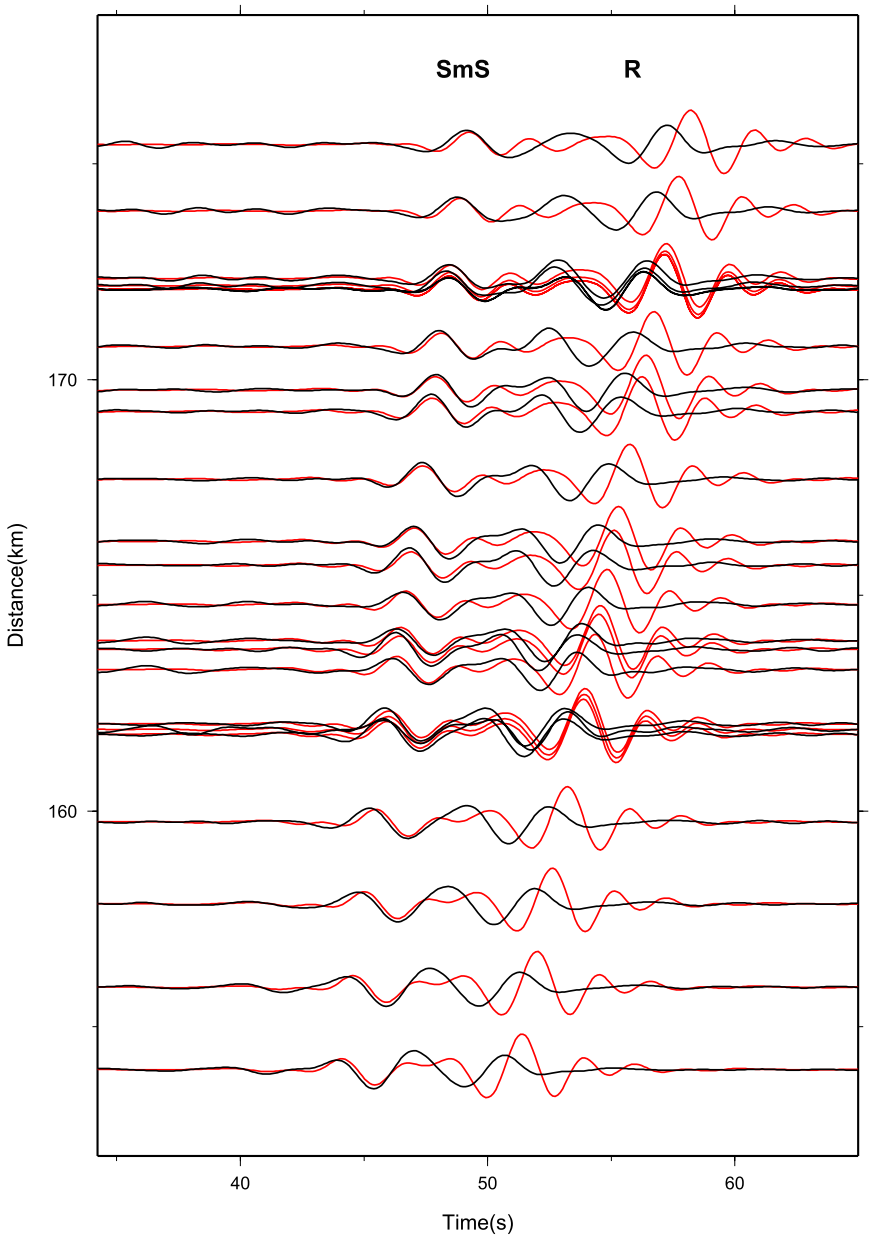


Figure 3.9: Observation of *SmS* in NCFs (bandpassed 2–5 s) of station pairs with A16 as pseudo source station. A16 is the closest CANOE station to YKA used in this study (150–180 km). At this distance range, the $SmS^2$ has not reached the critical reflection distance, and SmS is the strongest body wave phase. The black and red lines are the NCFs and synthetic seismograms computed with the 1-D model in Figure 3.7, respectively. The disagreement of Rayleigh waves is probably due to the lateral change of shallow structure.

## 3.5 Surface wave precursors caused by local noise anomaly

The density of stations in the Great Slave region allows a detailed record section to be constructed with over 400 NCFs (as displayed in Figure 3.10 at period bands 2–10 s and 1–2 s). The positive side and negative side have been folded and summed. For 1–2 s period band, the body wave arrivals have the same travel times as in 2–10 s period band while the Rayleigh waves are delayed due to dispersion. This increases the $SmS$ and $SmS^2$ separation from the Rayleigh waves in the 1–2 s period band, hence easier to identify. On the other hand, the stronger attenuation due to the increase of frequency content decreases the coherence between stations, which makes the NCFs much noisier. Consequently, in the following, we will concentrate on the 2–10 s period band. As expected for typical triplication behaviour, the record section shows that $SmS$ is strong in the distance range 150–180 km, while $SmS^2$ emerges beyond 280 km. Hence, the window near 250 km should be relatively free of strong body waves (Figure 3.10). The station pairs between A14 and YKA (solid purple line in Figure 3.6) are in this window. Figure 3.11 shows their stacked NCFs for November and December of 2004 with both positive and negative sides present. The NCFs of the summer seasons are not used here because the strong teleseismic $P$-wave energy from storms in the southern hemisphere causes strong artefacts near zero lag time (Gerstoft et al. 2008). As they appear outside the time window in which local body wave phases may be present, they are not discussed here. In Figure 3.11, besides the surface waves shown by the red arrows, clear arrivals persist before the surface waves. The most visible ones are denoted by blue arrows on each side. Note that the precursors on two sides are not symmetric in waveform or travel time. The precursors denoted by blue arrows on the positive side have much longer durations than those on the negative side. Similar precursors can be observed in many previous ASN studies (Shapiro et

al. 2005; Yao et al. 2006; Lin et al. 2008), but their source has not been identified.

The dense Yellowknife array enables us to have a closer look at these precursors. They appear to be coherent over the entire array, which means they are probably caused by some physical feature. The YKA consists of two perpendicular legs as shown in Figure 3.6. In Figure 3.11, the NCFs between A14 and Yellowknife stations on the east-west leg are coloured in blue, with the north-south leg in red. The precursors on the negative side have a different moveouts on the east-west leg than on the north-south leg, as denoted by the dash lines. More quantitatively, Figure 3.12 shows a detailed frequency-wavenumber (FK) analysis (Rost & Thomas 2002) for precursors on both the positive and negative sides. Blue arrows are their velocity vectors while red arrows are velocity vectors of corresponding direct surface waves. A comparison between these two FK plots shows that these precursors have surface wave velocity (blue and red arrows have similar length). They are not travelling along the great-circle path as the blue arrows have a different azimuth than the red arrows. Because these arrivals are precursors, they must have originated from anomalous noise sources because scattered surface waves would arrive after the direct Rayleigh wave. In particular, their azimuths as obtained by the FK analysis and absolute travel times which is the difference of travel times from the noise source anomaly (NSA) to the two stations allow these NSAs to be located (see the schematic in Figure 3.13). The two NSAs determined above are shown as purple dots in Figure 3.6.

We can determine additional locations of NSAs by examining more time windows of the NCFs. They are shown as yellow dots in Figure 3.6 and clearly cluster into two groups. One group concentrated near the Yellowknife array, while the other is more dispersed in a region to the south of the large topographic feature called the Horn Plateau. The first group of dots coincide with locations of several mining explosions (inset of Figure 3.6), hence probably indicates a noise anomaly generated by mining processes. Although these explosions have been diminished before cross correlation

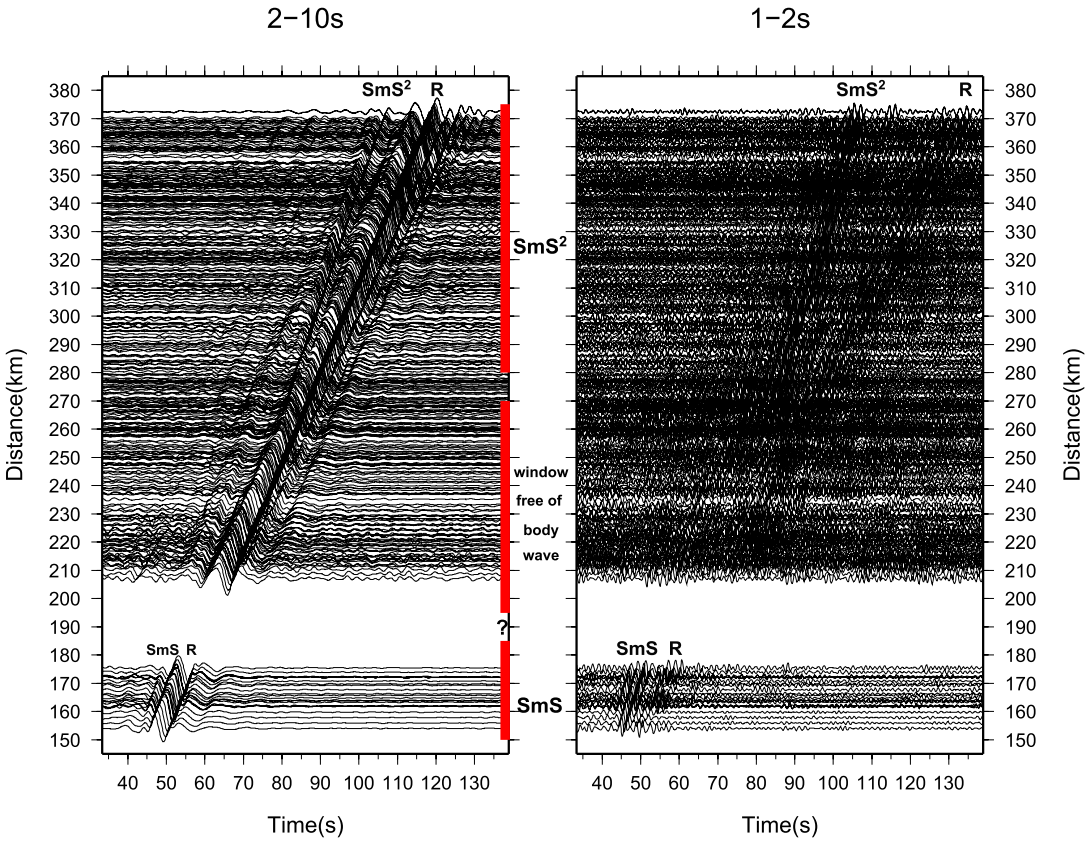


Figure 3.10: (Left panel) Complete record section of over 400 NCFs between CANOE array and Yellowknife array. NCFs have been bandpass filtered between 2 and 10 s. The positive side and the negative side are summed. *SmS* dominates $SmS^2$ at shorter distance range but $SmS^2$ dominates at larger distances as expected for a typical triplication behaviour. Between these two ranges, there is a window between 200 and 270 km relatively free of body waves. But clear signals still persist before surface waves (surface wave precursors), which are discussed in the text. (Right panel) Complete record section of NCFs for 1–2 s period band. Although much noisier, $SmS^2$ and Rayleigh waves can still be recognized. Although $SmS^2$ keeps its travel time the same as in 2–10 s period band, the Rayleigh waves are delayed because of dispersion as discussed earlier. SmS is actually cleaner because the amplitude of surface wave becomes much smaller.

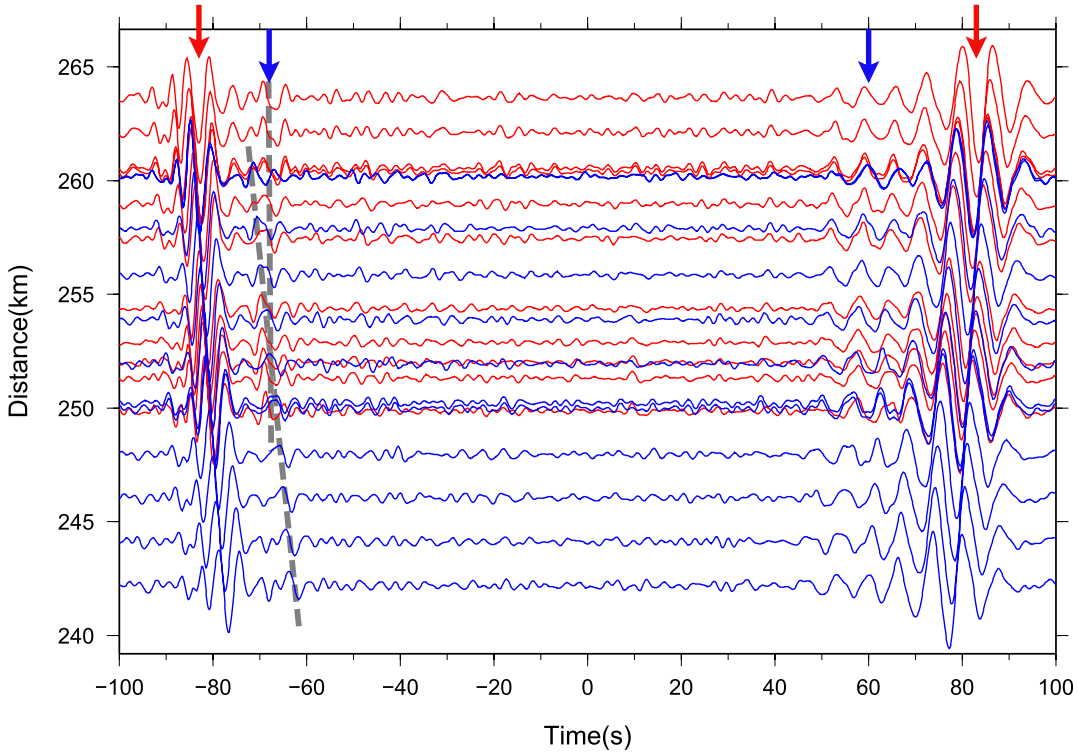


Figure 3.11: Observation of clear and coherent surface wave precursors in NCFs (2–10 s) between A14 and YKA stations for 2004 November and December at a distance of 250 km. At this distance range (about 250 km apart), $SmS$ and $SmS^2$ are weak compared with Rayleigh waves (shown by the red arrows). However, we can still observe clear signals arriving before Rayleigh waves (surface wave precursor), for example the signals marked by the blue arrows. These precusors are coherently present in NCFs between A14 and YKA stations. Note that the positive sides and negative sides of NCFs are not symmetric, which is probably because of the difference of noise from Pacific Ocean and Atlantic Ocean.

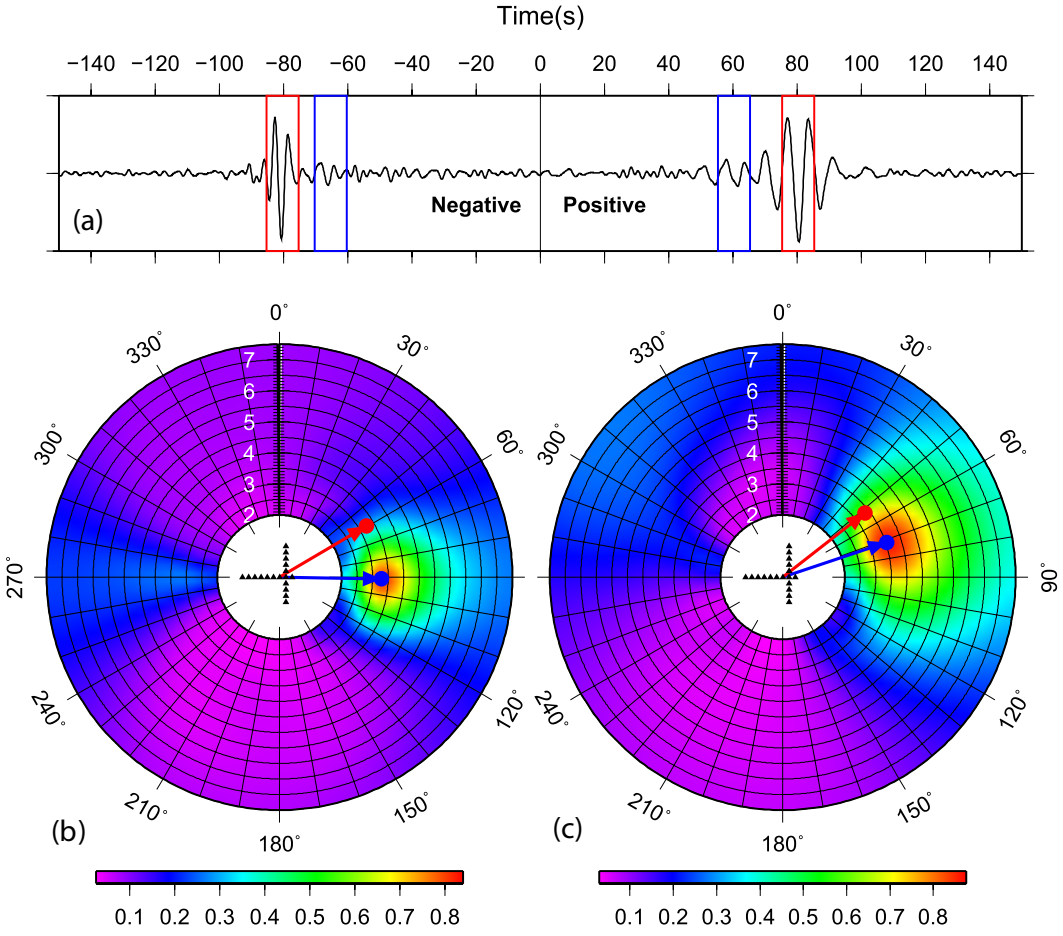


Figure 3.12: Locating NSAs with sliding-window frequency–wavenumber (FK) analysis (Rost & Thomas 2002) of surface wave precursors. (a) Shows one example of NCF between A14 and YKR7. Because of the precursors coherence shown in Figure 3.11, we can measure their apparent velocity vector defined by propagation azimuth and apparent velocity with Sliding-Window FK analysis. Results for the two windows defined by blue boxes are shown in (b) and (c), respectively. The background colour is normalized power of stacked signals (Rost & Thomas 2002). The blue arrows are the optimal apparent velocity vectors and blue dots show the corresponding velocities and azimuths. For comparison, the apparent velocity vectors for Rayleigh waves (red boxes) are also plotted as red arrows and red dots. We can see that the blue arrows have very close velocities (lengths) to red arrows (from Rayleigh waves), but quite different azimuths. This means that the precursors are not body waves, but surface waves travelling off the great circle.

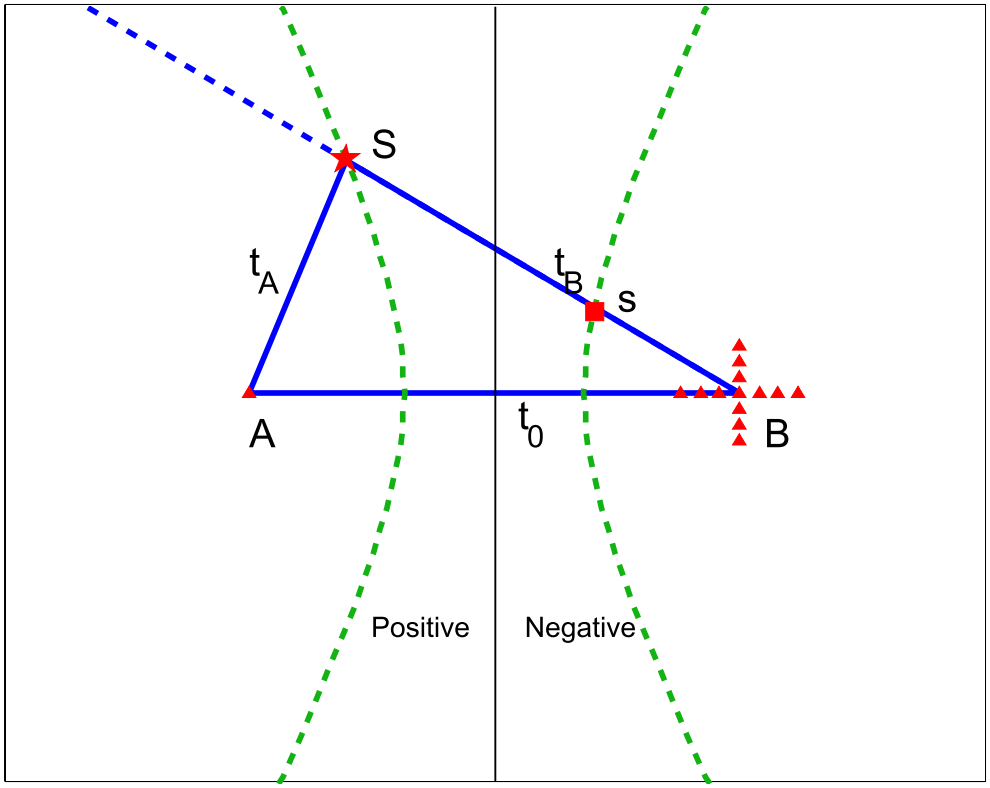


Figure 3.13: Noise source anomaly (NSA) and method to localize an NSA. Suppose we have a scenario shown in this figure, where red triangles are stations. $B$ is an array with stations $B_i$. An NSA at point $S$ (uniform part already subtracted) emits surface wave noise continuously. It will be recorded at station $A$ with a delay $t_A$, array station $B_i$ with a delay $t_{B_i}$. The NCFs between station A and array stations $\mathrm{B_i}$ will have a signal at $t_{B_i} - t_A$. As $t_{B_i} - t_A$ is always smaller than $t_0$, the signal arrives earlier than the surface wave Green's function (surface wave precursor). It should be noticed that the relative travel times of this signal across the $B$ array do not change after cross correlating with station $A$. This enables us to use FK to determine the azimuth of the NSA (dash blue line in the figure). Assuming the similarity of waveforms recorded at station $A$ and the array, the absolute time of maximum cross correlation is $t_{B_i} - t_A$, which requires the NSA on a hyperbola (green dash lines in the figure). These two steps lead to two possible locations of the NSA, shown as $S$ (red star) and s (red squares). They can be distinguished by whether the precursor appears on the positive or negative side of NCFs.

by temporal normalization (Bensen et al. 2007), the continuous noise generated by the mine cannot be removed. The second group of NSAs lies in the wind shadow (with much lower wind speed than surrounding area) of the Horn Plateau (Canada Environment 2009), as the dominant wind direction in this area is from north to south. We suggest that this group of NSAs is generated by an absence of wind-land-interaction (i.e., a void) in the assumed uniformly distributed noise sources. A synthetic to support this is shown in Figure 3.14, where a void of noise sources from azimuth 40° to 50° causes a surface wave precursor in the NCF.

## 3.6 Discussion and Conclusion

As shown by Weaver & Lobkis (2001), the equipartitioning of the Earth's normal modes in noise will allow us to obtain the complete Green's function between two stations. However, as pointed out by Snieder (2004), the fact that almost all of the noise sources are distributed on the Earth surface means fundamental surface wave modes contain most of the energy. Theoretical studies by Wapenaar (2004, 2006), Snieder (2004) and Fan & Snieder (2009) show that to obtain the fundamental mode surface wave part of the Green's function, the distribution of noise source on the free surface is enough. However, for body wave phases, such as reflections, noise sources at depth are necessary. This seems to mean that body wave phases are not retrievable from seismic noise as almost all the noise sources are on the free surface. However, they also pointed out that inhomogeneous structure of the Earth may be helpful to fix this difficulty. For example, Snieder (2004) treat the subsurface discontinuity as a mirror to create mirror-source at depth. Until now, it is still not clear whether we can get the body wave part of the Green's function or even the complete Green's function from this surface-generated seismic noise. The weak amplitude of body wave phases in the Green's function make the problem even harder. As stations are on the

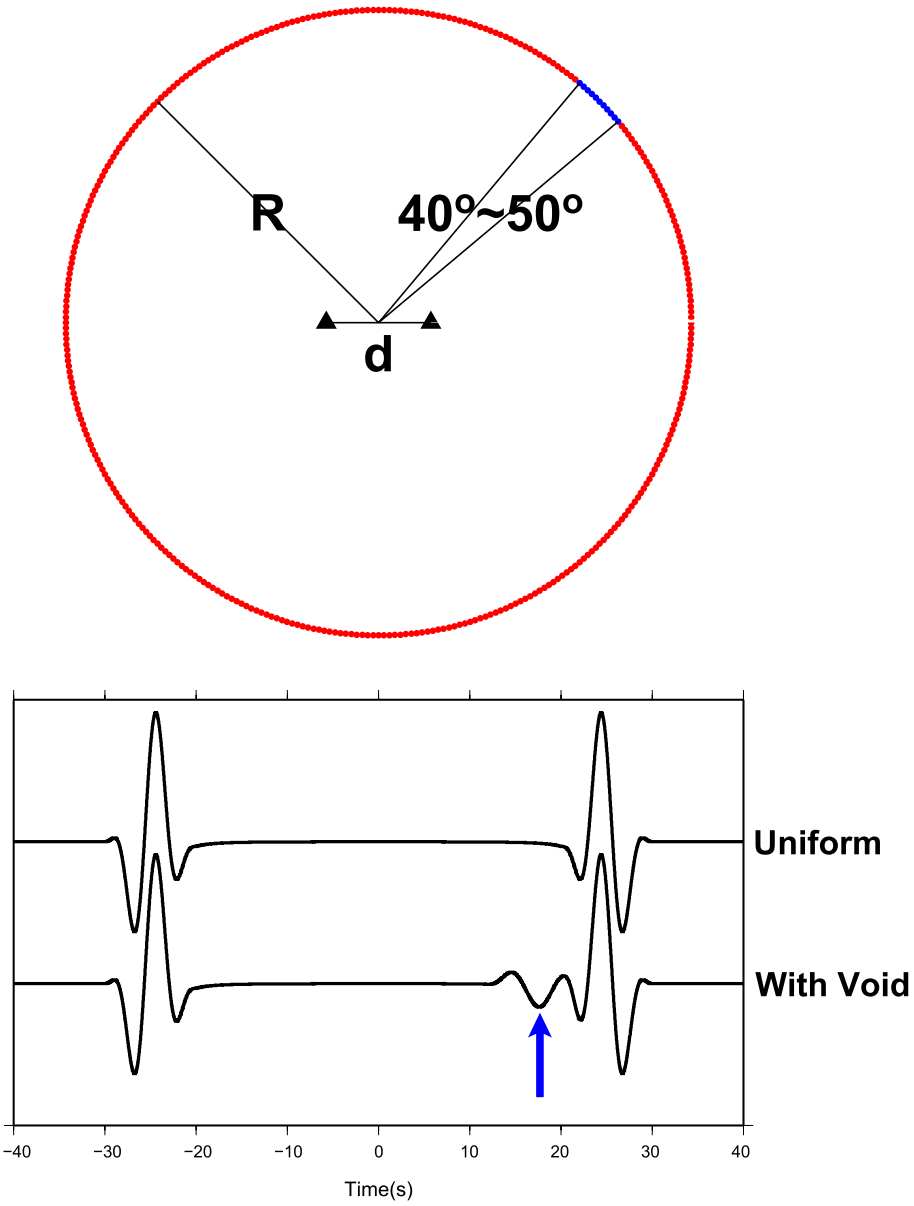


Figure 3.14: Two stations separated by $d$=100 km are surrounded by a circle of noise sources ($R$=300 km). We simulated two cases here: (1) noise sources distribute uniformly on the circle; (2) same as (1) except that the noise sources between 40° and 50° (blue part in figure) are taken off. The corresponding synthetic NCFs at 5 s period are shown in lower panel. The void of noise sources causes a surface wave precursor on the NCF, marked by the blue arrow.

free surface, we expect the Green's function to be similar to the solution to Lamb's problem in which the surface wave is an order of magnitude larger than the body waves.

In this paper, by array analysis of NCFs in cratons with simple crustal structures, we show that the noise cross correlation technique now can detect certain body wave phases when they have comparable strengths in certain conditions ($SmS^{\mathrm{n}}$ near their critical distances in our examples). The reason for strong SmS and its multiples to be observed from ASN could be that noise sources are distributed in the whole crust instead of just being near the free surface. Being the most heterogeneous part of the Earth, crust consists of scatterers at many scales and strongly scatters waves with resonant wavelength. Moreover, because of the lower velocity, crust behaves as a wave guide channel trapping most of the body wave energy inside, which explains dominant *Lg* waves for regional crustal earthquakes and should also be expected for ambient seismic noises (Kennett 1984; Kennett & Mykkeltveit 1984). Indeed array analysis by Koper et al. (2009) supports that strong energy of short period seismic noise propagates as *Lg* waves. Cormier & Anderson (2004) argues that Lg wave is dominated by multiple *SmS* arrivals. This means that there is sufficient energy in the noise field trapped between the surface and the Moho to allow the retrieval of body waves in the short period band.

Scattering due to topography or microbasins (very thin basins) could be another mechanism of converting wave field of dominant surface wave into wave field of both surface wave and body wave, as observed and modelled by Clouser & Langston (1995). In their study, Rayleigh waves are proposed to be generated by teleseismic $P$ waves. According to reciprocity, $P$ waves can also be expected by Rayleigh waves scattered by topography. Although topographic variation in cratons are fairly weak, microbasins may serve as strong scatterers (Stead & Helmberger 1988).

Other body wave phases are probably present, but masked by the persistent sur-

face wave precursors due to uneven distribution of noise sources. These noise source anomalies could be human activities, wind–topography and other solid–fluid interactions of the Earth, such as storms (Bromirski 2009). By numerical simulation Lin et al. (2008) shows that as long as the strength of the noise source varies smoothly versus azimuth, the bias to the surface wave Green's function is negligible. The broad microseism source area and scattering may contribute to this smooth variation. However, as shown by this paper, nearby noise source anomaly may not have such a smooth variation because of high heterogeneity of distribution and lack of scattering over short distances. Better understanding of the noise sources, especially these local noise source anomalies will help suppress the contaminating surface wave precursors to get the complete Green's functions from the NCFs. Also, as *SmS* can be much stronger than surface waves around 1 s, detailed analysis of NCF in this frequency band can provide a valuable tool for site amplification mapping.

## Acknowledgments

The authors thank the operators of the Southern Africa Seismic Experiment and CANOE array, IRIS, Earthquakes Canada for providing data used in this study. We acknowledge Ronald M. Clowes and Gabriela Fernandez Viejo for providing the velocity model of Great Slave region. The suggestions from two reviewers were very helpful to improving the paper. This work was supported by NSFC 40674027 and CAS fund kzcx2-yw-116-01 and by USGS Award #G09AP0082 at California Institute of Technology.

## References

Bensen, G.D., Ritzwoller, M.H., Barmin, M.P., Levshin, A.L., Lin, F., Moschetti, M.P., Shapiro, N.M. & Yang, Y., 2007. Processing seismic ambient noise data

to obtain reliable broad-band surface wave dispersion measurements, Geophys. J. Int., 169(3), 1239–1260.

Bensen, G.D., Ritzwoller, M.H. & Shapiro, N.M., 2008. Broadband ambient noise surface wave tomography across the united states, J. geophys. Res., 113(B5), B05306, doi:10.1029/2007JB005248.

Bostock, M.G., 1998. Mantle stratigraphy and evolution of the Slave province, J. Geophys. Res., 103(B9), 21183–21200, doi:10.1029/98JB01069.

Bromirski, P.D., 2009. Earth vibrations, Science, 324(5930), 1026–1027.

Canada Environment, 2009. Wind atlas of Canada. Available at:http://www.windatlas.ca/, accessed on 2009 December 1.

Clouser, R.H. & Langston, C.A., 1995. Modeling P–Rg conversions from isolated topographic features near the Noress array, Bull. seism. Soc. Am., 85(3), 859–873.

Clowes, R.M., Hammer, P.T.C., Fernandez-Viejo, G. & Welford, J.K., 2005. Lithospheric structure in northwestern Canada from lithoprobe seismic refraction and related studies: a synthesis, Can. J. Earth Sci., 42(6), 1277–1293.

Cormier, V.F. & Anderson, T.S., 2004. Efficiency of Lg propagation from SMS dynamic ray tracing in three-dimensionally varing crustal waveguides, Pure appl. Geophys., 161, 1613–1633.

Draganov, D., Wapenaar, K., Mulder, W., Singer, J. & Verdel, A., 2007. Retrieval of reflections from seismic background-noise measurements, Geophys. Res. Lett., 34(4).

Draganov, D., Campman, X., Thorbecke, J., Verdel, A. & Wapenaar, K., 2009. Reflection images from ambient seismic noise, Geophysics, 74(5), A63–A67.

Dziewonski, A., Bloch, S. & Landisma, M., 1969. A technique for analysis of transient seismic signals, Bull. seism. Soc. Am., 59(1), 427–444.

Fan, Y. & Snieder, R., 2009. Required source distribution for interferometry of waves and diffusive fields, Geophys. J. Int., 179(2), 1232–1244.

Gerstoft, P., Shearer, P.M., Harmon, N. & Zhang, J., 2008. Global P, PP, and PKP wave microseisms observed from distant storms, Geophys. Res. Lett., 35(23), L23306, doi:10.1029/2008GL036111.

James, D.E., Niu, F.L. & Rokosky, J., 2003. Crustal structure of the Kaapvaal craton and its significance for early crustal evolution, Lithosphere, 71(2-4), 413–429.

Kennett, B.L.N., 1984. Guided wave-propagation in laterally varying media. 1. Theoretical development, Geophys. J.R. astr. Soc., 79(1), 235–255.

Kennett, B.L.N. & Mykkeltveit, S., 1984. Guided wave-propagation in laterally varying media. 2. Lg-waves in northwestern Europe, Geophys. J. R. astr. Soc., 79(1), 257–267.

Koper, K.D., De Foy, B. & Benz, H.M., 2009. Composition and variation of noise recorded at the Yellowknife seismic array, 1991–2007, J. geophys. Res., 114, B10310.

Levshin, A.L. & Ritzwoller, M.H., 2001. Automated detection, extraction, and measurement of regional surface waves, Pure appl. Geophys., 158(8), 1531–1545.

Lin, F.C., Moschetti, M.P. & Ritzwoller, M.H., 2008. Surface wave tomography of the western United States from ambient seismic noise: Rayleigh and love wave phase velocity maps, Geophys. J. Int., 173(1), 281–298.

Ma, S., Prieto, G.A. & Beroza, G.C., 2008. Testing community velocity models for southern California using the ambient seismic field, Bull. seism. Soc. Am., 98(6), 2694–2714.

Mercier, J.P., Bostock, M.G., Audet, P., Gaherty, J.B., Garnero, E.J. & Revenaugh, J., 2008. The teleseismic signature of fossil subduction: northwestern Canada, J. geophys. Res., 113(B4), 16, B04308, doi:10.1029/2007JB005127.

Mori, J. & Helmberger, D., 1996. Large-amplitude Moho reflections (SmS) from landers aftershocks, southern California, Bull. seism. Soc. Am., 86(6), 1845–1852.

Prieto, G.A. & Beroza, G.C., 2008. Earthquake ground motion prediction using the ambient seismic field, Geophys. Res. Lett., 35(14).

Rost, S. & Thomas, C., 2002. Array seismology: methods and applications, Rev. Geophys., 40(3), 27, 1008, doi:10.1029/2000RG000100.

Roux, P., Sabra, K.G., Gerstoft, P., Kuperman, W.A. & Fehler, M.C., 2005. P-waves from cross-correlation of seismic noise, Geophys. Res. Lett., 32(19), L19303, doi:10.1029/2005GL023803.

Shapiro, N.M., Campillo, M., Stehly, L. & Ritzwoller, M.H., 2005. High-resolution surface-wave tomography from ambient seismic noise, Science, 307(5715), 1615–1618.

Snieder, R., 2004. Extracting the Green's function from the correlation of coda waves: a derivation based on stationary phase, Phys. Rev. E, 69(4), 046610.

Stead, R.J. & Helmberger, D.V., 1988. Numerical-analytical interfacing in two dimensions with applications to modeling NTS seismograms, Pure appl. Geophys., 128(1–2), 157–193.

Stehly, L., Campillo, M. & Shapiro, N.M., 2006. A study of the seismic noise from its long-range correlation properties, J. Geophys. Res., 111, B10306, doi:10.1029/2005JB004237.

Stehly, L., Fry, B., Campillo, M., Shapiro, N.M., Guilbert, J., Boschi, L. & Giardini, D., 2009. Tomography of the alpine region from observations of seismic ambient noise, Geophys. J. Int., 178(1), 338–350.

Viejo, G.F. & Clowes, R.M., 2003. Lithospheric structure beneath the Archaean slave province and proterozoic Wopmay Orogen, northwestern Canada, from a lithoprobe refraction/wide-angle reflection survey, Geophysical Journal International, 153: 1–19. doi: 10.1046/j.1365-246X.2003.01807.x

Wapenaar, K., 2004. Retrieving the elastodynamic Green's function of an arbitrary inhomogeneous medium by cross correlation, Phys. Rev. Lett., 93(25), 254301.

Wapenaar, K., 2006. Green's function retrieval by cross-correlation in case of one-sided illumination, Geophys. Res. Lett., 33(19), L19304, doi:10.1029/2006GL027747.

Weaver, R.L. & Lobkis, O.I., 2001. Ultrasonics without a source: thermal fluctuation correlations at MHz frequencies, Phys. Rev. Lett., 87(13), 4, 134301.

Yang, Y.J. & Ritzwoller, M.H., 2008. Characteristics of ambient seismic noise as a source for surface wave tomography, Geochem. Geophys. Geosyst., 9, Q02008, doi:10.1029/2007GC001814.

Yang, Y.J., Ritzwoller, M.H., Levshin, A.L. & Shapiro, N.M., 2007. Ambient noise Rayleigh wave tomography across Europe, Geophys. J. Int., 168(1), 259–274.

Yao, H.J., Van Der Hilst, R.D. & De Hoop, M.V., 2006. Surface-wave array tomography in Se Tibet from ambient seismic noise and two-station analysis. I. Phase velocity maps, Geophys. J. Int., 166(2), 732–744.

Zhang, J., Gerstoft, P. & Shearer, P.M., 2009. High-frequency P-wave seismic noise driven by ocean winds, Geophys. Res. Lett., 36, L09302, doi:10.1029/2009GL037761.

Zheng, S.H., Sun, X.L., Song, X.D., Yang, Y.J. & Ritzwoller, M.H., 2008. Surface wave tomography of China from ambient seismic noise correlation, Geochem. Geophys. Geosyst., 9, Q05020, doi:10.1029/2008GC001981.

Zhu, L.P. & Helmberger, D.V., 1996. Advancement in source estimation techniques using broadband regional seismograms, Bull. seism. Soc. Am., 86(5), 1634–1641.

Zhu, L.P. & Rivera, L.A., 2002. A note on the dynamic and static displacements from a point source in multilayered media, Geophys. J. Int., 148(3), 619–627.